An Alternative Design Space for High-Power Wick-Type Evaporators for Electronics Cooling

Katherine Piper[a,*], Scott N Roberts[b]

[a]Department of Civil and Environmental Engineering, Carnegie Mellon University, Pittsburgh, PA 15213 USA
[b]Jet Propulsion Laboratory, California Institute of Technology, Pasadena, CA 91109, USA

Abstract

High power spacecraft have long relied on Loop Heat Pipes (LHPs) for passive thermal management. Performance of LHPs and other evaporative cooling systems has historically been governed by a porosity/ permeability tradeoff, which both limits performance and constrains manufacturing approaches. In this work, we unify prior models of wetting, meniscus formation, and capillary evaporation, to demonstrate these surface phenomena act as independent, separately tunable parameters governing evaporator performance, decoupled from bulk porosity and permeability. This independence enables large-pore wicks with reduced risk of clogging and a wider range of lower-cost manufacturing methods, including additive manufacturing. In a direct comparison between evaporators with identical bulk wick properties, our optimized approach provides a 42% performance improvement in conductance while maintaining the cost savings of additive manufacturing and the flight-proven long term reliability of LHPs. These results establish a pathway for additively manufactured, high-performance, low-cost passive evaporators, addressing manufacturing constraints that have limited LHP deployment in terrestrial applications such as electronics thermal management and waste heat recovery.

Keywords: Two-Phase Heat Transfer, Capillary Evaporation, Additive Manufacturing, Loop Heat Pipes, Thermal Management

1. Introduction

The growing power requirements of AI datacenters has recently drawn attention to the parasitic electrical demands of computer cooling systems. With global datacenter electricity demands projected to exceed 1000TWh by 2030[1], the development of more efficient electronics cooling systems is an imminent need[2]. Existing cooling systems, such as pumped liquid loops, do not always meet the cooling demands of modern computing architectures[3, 4], and, in datacenters, result in high noise pollution, water use, and overall community impact[5]. While two-phase heat transfer has been widely studied for high-power applications[6–9], device-scale implementation of two-phase cooling presents an array of engineering challenges. Heat pipes, vapor chambers, and other common passive two-phase devices are only capable of transporting heat over small distances[10–12]. In long distance two-phase loops, a high quality metal sintered wick, frequently with a pore size on the order of $1\mu m$, creates separation between liquid and vapor phases, which enables highly efficient long distance heat transfer.

Loop Heat Pipes (LHPs) are one class of fully passive long-distance two phase loop which use these micro porous wicks (Figure 1(a)). In microgravity, LHPs are capable of transferring heat a distance of several meters, while, when oriented horizontally in a gravitational field, LHPs are capable of passively transferring

*Corresponding author and Lead Contact
Email addresses: kbpiper@andrew.cmu.edu (Katherine Piper), scott.n.roberts@jpl.nasa.gov (Scott N Roberts)

heat loads tens of meters. Prior studies indicate LHP performance is primarily dependent on the quality and structure of this porous wick, which, in addition to its role in evaporation and fluid transport, must have a small pore size to maintain a pressure gradient between liquid and vapor phases, and must have high permeability to maximize fluid flow rate. This tradeoff between porosity and permeability, as well as a diverse array of manufacturing and assembly challenges has traditionally resulted in a high cost device[13, 14], rarely implemented outside of high-budget space missions, such as GOES and EOS satellites, Boeing 702, and JPL's Farside Seismic Suite. Low-cost LHPs have been developed for industrial uses in LED street lighting and thermoelectric coolers[15], however this implementation is primarily limited to small heat fluxes and short distances[16]. In research applications, LHPs have been studied for highly efficient cryogenic cooling[17, 18] and have demonstrated potential for up to 30% cooling system power savings in datacenters [19, 20]. Metal 3D printing, which fabricated the structure in Figure 1(b), offers a resolution to some of the manufacturing challenges, significantly reducing the cost of the device, however the additive process results in a low-quality sintered wick, limiting device performance.

Recent work in surface evaporation from architected porous structures has demonstrated the significant impact of interfacial effects on rate of evaporation[6, 21, 22], however, these metasurface wicks are unable to maintain the pressure gradient required in LHPs. This work builds on these advances in interfacial evaporation, models for evaporation from individual capillary tubes[23–25], and our advances in metal additive manufacturing[26–28] to access a novel design space for improving additively manufactured LHP evaporator performance. While traditional LHP performance optimization is focused on developing wicks with small pore size, high porosity, and high permeability[29], single-piece additively manufactured evaporators readily enable optimization of the surface effects governing wick evaporation, shown in Figure 1(c).

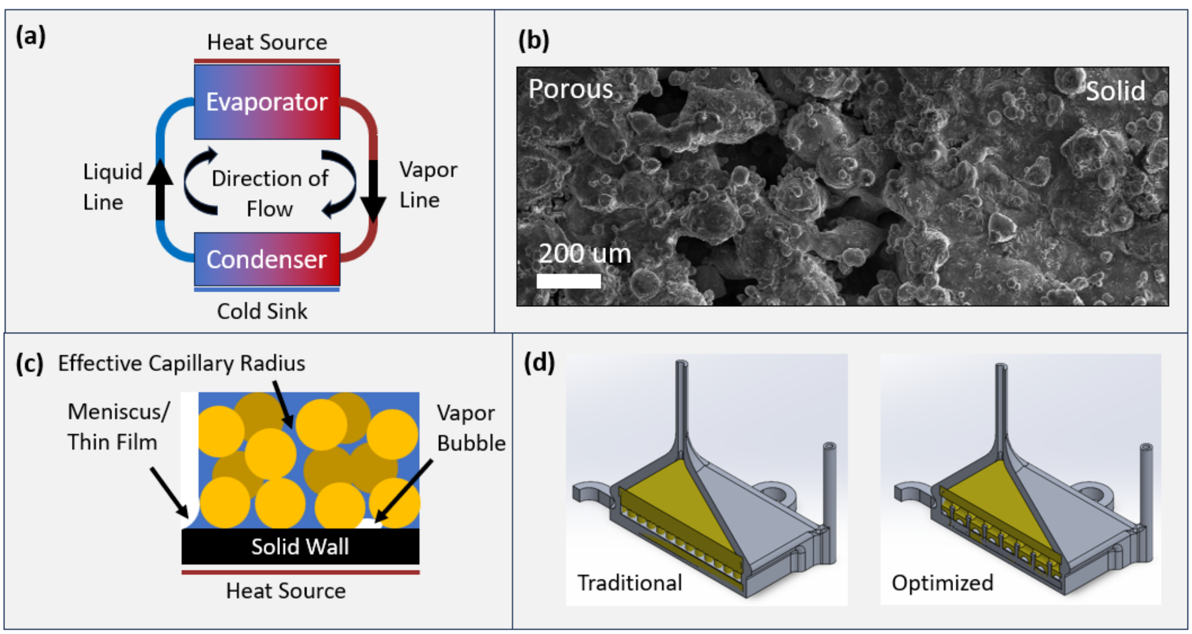

Figure 1: (a) A basic diagram of a loop heat pipe (b) SEM of the porous/solid interface in an additively manufactured evaporator (c) A porous wick diagram with our critical parameters identified (d) CAD of our traditional and optimized evaporator designs

We present an engineering design framework which delivers a 42% average performance improvement in conductance of high-performance LHP evaporators, while maintaining a 2-week design/manufacture/test lead time, and less than 7% performance variance across samples, in contrast to traditional sintered wicks, which have published variance as high as 50%[30]. To demonstrate this framework in a controlled manner, we fabricate and test two devices with identical wick porosity and permeability. One device incorporates a conventional wick geometry representative of current practice, and the second incorporates a heuristically optimized cross-section geometry and architected interfacial characteristics aiming to maximize evaporation rate without sacrificing capillary pressure (Figure 1(d)). Our results demonstrate wetting, meniscus formation, and capillary evaporation are independent, dominant, and previously underexploited tunable performance variables in microporous wick design, and the conventional design framework omits a significant mechanism amenable to optimization using emerging manufacturing methods.

2. Loop Heat Pipes

LHPs are self-contained, passive, high-performance heat transfer devices. Due to a range of manufacturing constraints and costs, high-performance LHPs are traditionally used exclusively in applications where both weight and power efficiency are at a premium. In its most basic form, an LHP consists of an evaporator, where a liquid refrigerant is converted to vapor, and a condenser, where the vapor is converted back to liquid. The evaporator and condenser are linked by several meters of thin adiabatic tubing. This basic cycle is shown in Figure 2. Existing efforts to improve LHP performance have primarily focused on optimization of

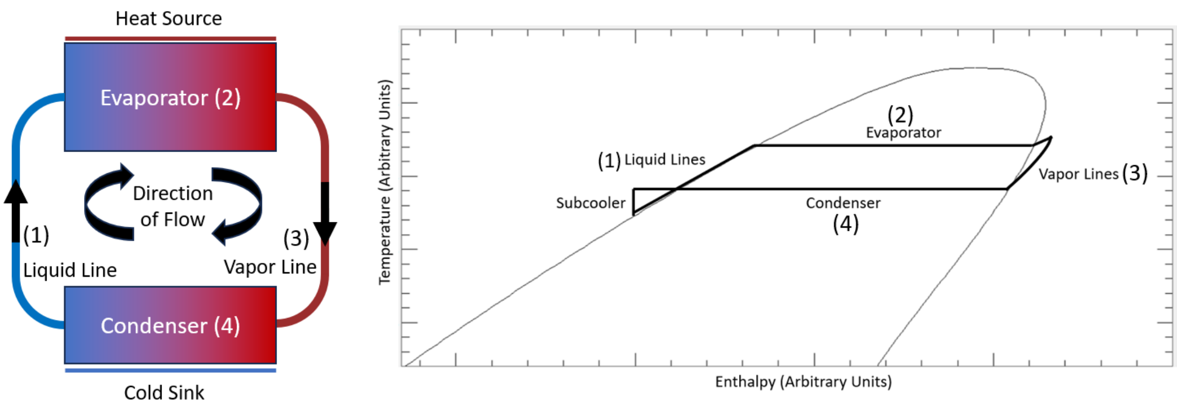

Figure 2: LHP flow schematic and temperature-enthalpy thermodynamic cycle

porosity, permeability, and other bulk wick properties through optimization of particle size and manufacturing process[31, 32], while reviews have acknowledged the potential for significant improvements through additive manufacturing[33–35]. The traditional process for producing LHPs consists of precision manufacturing individual components and multiple assembly steps. The porous wick, typically made of titanium, nickel, stainless steel, or a range of other low thermal conductivity alloys, is produced via metal sintering, while the housing, often a high thermal conductivity material, is manufactured through traditional subtractive machining processes. The wick and housing are then assembled, and mated with a knife-edge seal to prevent unintended flow between the vapor and liquid regions of the evaporator[14, 36, 37]. While advanced wick design concepts have been discussed in the literature[31, 34, 37], this traditional manufacturing process limits the possible shapes an LHP can be fabricated in, and the most common LHP evaporator design is concentric, where the wick and housing both have circular cross sections. Recent advances have included a range of novel manufacturing methods for wicks[31, 33, 38], as well as flat geometries designed to better accommodate heat sources such as CPUs[32, 39, 40]. A simplified diagram of a traditional LHP evaporator is shown in Figure 3a. This manufacturing process is expensive due to several precision steps and yield losses, traditionally limiting the application of LHPs to these large budget space missions. Advances in additive manufacturing have enabled lower cost LHP manufacturing through two competing approaches. First, architected wicks have been manufactured using small-scale CAD defined features and powder bed fusion processes[38, 41]. Separately, by applying "Lack of Fusion" (LoF) selective laser melting print parameters, low-cost additively manufactured wicks have been developed with improved porosity and permeability versus CAD-defined wicks, while sacrificing some control over the precise porous geometry[35, 42]. LoF porous wicks allow for print-in-place evaporators, which do not require an assembly step, however the wick and housing must be made of the same material, and the porous wick generally has lower permeability and lower porosity than wicks fabricated through the traditional sintering process[26]. Despite these limitations, significant performance improvements are made available by skipping the assembly step, enabling evaporator geometries which cannot be assembled. An example diagram of a geometry-conforming evaporator is shown in Figure 3b. In addition to the performance improvements enabled through geometry-conforming LHPs, the additive

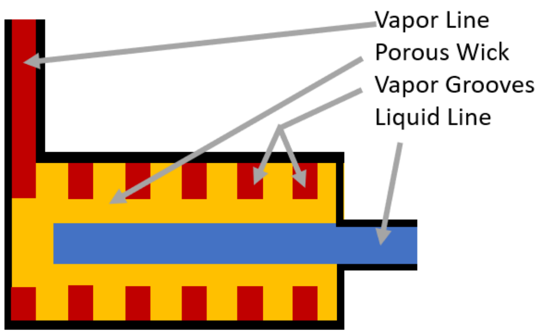

(a) A schematic cross section of a traditional circular LHP evaporator

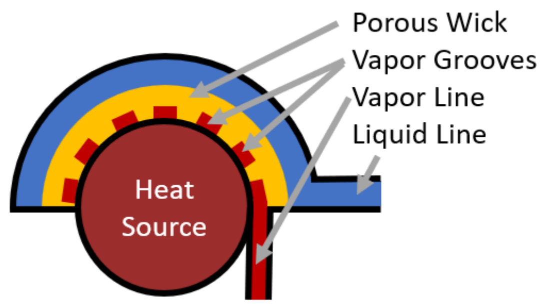

(b) A schematic cross section of a geometry-conforming LHP evaporator

Figure 3: Comparison of LHP evaporator geometries

manufacturing process enables multiscale optimization of the surface evaporation parameters at the wick/solid interface, a design optimization previously neglected in the literature[34].

3. Model Development

While the physics governing evaporation from capillary tubes has been well documented in prior work[23, 24, 43], and recent work has extended these models to metasurface wicks[21, 22], these advances have seen limited application to evaporative, closed loop two-phase cooling systems, where a focus on porosity and permeability remains dominant. We extend this work in capillary evaporation to additively manufactured porous wicks, aiming to specifically tailor the porous/solid interface to maximize rate of heat transfer of an evaporating meniscus across low power, medium power, and high power operational regimes.

3.1. The LHP Thermodynamic Cycle

The thermodynamics of an LHP are driven by an evaporation/condensation cycle, where liquid evaporates at the surface of the hot side of the wick, is routed through an adiabatic section, and then arrives at the condenser, where the vapor changes to liquid before returning to the evaporator. Because an LHP operates as a pure, single compound fluid system, both evaporation and condensation occur on the liquid/vapor saturation curve, with minimal superheat and subcooling occurring in the evaporator and condenser. A detailed thermodynamic analysis of the cycle is provided by Hamdan (2009)[44]. Additional components, such as a compensation chamber, are often present to accommodate variations in heating power and improve operating characteristics. For a pure fluid, the most basic analysis of energy transfer in evaporation is $\dot{q} = \frac{\dot{m}}{\Delta H_v}$, where $\dot{q}$ is the rate of heat transfer, $\dot{m}$ is the mass flow rate, and ΔH_v corresponds to the latent heat of vaporization, but there is no strict relationship to temperature. ΔH_v is determined by the thermophysical properties of the working fluid. $\dot{m}$ is typically directly correlated to wick properties, such as permeability and porosity, but, as highlighted earlier, is also dependent on the rate of evaporation from the wick[45].

The exact principles governing evaporation from an LHP wick vary across operational regimes, which include low-power, medium-power, and high-power operation, shown in Figure 4. In low-power operation,

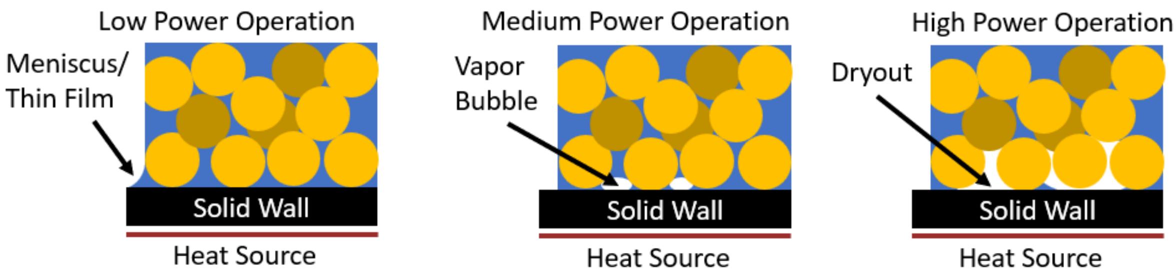

Figure 4: Fluid Flow at the Wick/Solid interface during three states of LHP operation

evaporation is dominated by liquid bridge formation at the interface between the solid and porous structure in the vapor grooves, while in medium and high-power operation, evaporation is instead dominated by vapor bubble formation at the interface between the porous wick and solid wall[40, 46]. Each of these regimes requires different techniques for modeling evaporation and its influence on $\dot{m}$. By combining these lessons, we demonstrate an engineering framework for optimization of the interfacial properties of an LHP, improving system performance by lowering the temperature of operation while maintaining a constant input power.

3.2. Performance Modeling

In practice, there is no clean dividing line between low and medium power operation of porous wicks, and meniscus/thin film evaporation and vapor bubble formation both occur up until the onset of dryout in high power operation. Therefore, a predictive performance model should account for both meniscus formation/thin film wetting and capillary heat flow. Meniscus formation/thin film wetting occurs primarily at the triple point contact region between the solid wall, the porous wick, and the open vapor channel. For a rough surface, such as an additively manufactured heat pipe wick with grooves larger than $5um$, experimental results find a contact angle $\theta > 90°$[31, 47], and, following the Wenzel Wetting model in this regime, reduced surface roughness will lead to improved wetting[48, 49]. While determining the exact contact angle requires precise experiment, Wenzel's model proposes a contact angle linearly proportional to $1/R_a$, the surface roughness, and, by geometric construction, the contact area available for heat transfer is also linearly proportional to $1/R_a$. Additionally important is L_{psv}, a measure of the total linear contact area between the porous wick, the solid housing, and the vapor channel, defining the total area in which a meniscus can form. This results in Equation 1, a predicted performance differential due to surface roughness and triple point contact area alone.

$$\frac{q_1}{q_2} = \frac{L_{psv,1}/R_{a_1}}{L_{psv,2}/R_{a_2}} \tag{1}$$

While thermal performance is dominated by solid surface wetting behavior at low powers, heat flux at higher powers is better modeled as a collection of capillary tubes. Models for capillary heat flow are well established, and demonstrate that total heat flow ($q_{channel}$) in the contact region is dependent on capillary number Ca, and independent of large scale geometry[23, 24]. Approximating a porous wick as a collection of capillary tubes, a simplification necessary to render a tractable modeling approach, allows us to approximate capillary heat flow in Equation 2.

$$q_{channel} = \frac{1}{\theta} \ln\left(\frac{2b}{\varepsilon\delta}\right) - \frac{2}{x_1} + ..., \qquad \theta = b\left(\frac{3Ca}{f}\right)^{1/4} [23] \tag{2}$$

In the above equation, b and δ are integration constants, f is a ratio of local pressure scales, and ϵ and x_1 are local length scales. For a full derivation of this formula and its independence from geometry, we refer the reader to Morris (2003)[23]. In general, $q_{channel} \propto 1/Ca$ as well as these geometry-dependent interfacial constants, however, in this work, we specifically focus on the difference in heat transfer between two wicks with identical porosity, permeability, and pore size distribution. For constant bulk wick properties, the capillary number (Ca, a measure of capillary forces in the wick) and geometric parameters ($b, \delta, \epsilon, x_1, f$) are constant, and we find $q_{total} = nq_{channel}$, where n is simply the number of pores contacting a solid surface as defined by large scale geometry. This leads to Equation 3, the expected performance ratio due exclusively to capillary evaporation, where A_{sq} refers to the porous/solid contact area, which is exactly linearly related to n, the quantity of channels.

$$\frac{q_1}{q_2} = \frac{A_{sq,1}}{A_{sq,2}} \tag{3}$$

Real additively manufactured wicks, shown with UV contrast and microCT in Figure 5, are more complicated than this homogenized model, however the homogenized prediction aligns with prior models of loop heat pipes[40], as well as experimental studies on unit-cell capillary evaporators[21].

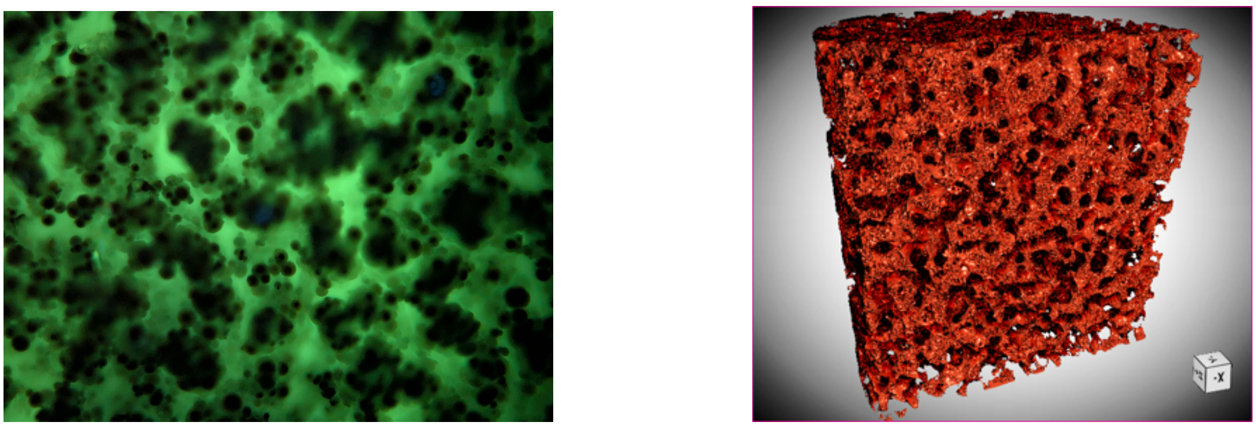

(a) UV Contrast imagery of porous wick, pores are filled with fluorescent dye

(b) Micro-CT imagery of porous network, pores are represented in red

Figure 5: The complex network of additively manufactured pores

For two devices with identical bulk wick properties, we expect the difference in performance q_1/q_2, to be bounded by these characteristics from Equations 1 and 3. Therefore, we expect to find a lower bound performance improvement as the minimum of these two effects, given in the left inequality of 4, and an upper bound to the performance improvement to be given by the product of these two effects, given by the right inequality of 4.

$$\min\left\{\frac{A_{sq,1}}{A_{sq,2}}, \frac{L_{psv,1}/R_{a_1}}{L_{psv,2}/R_{a_2}}\right\} \leq \frac{q_1}{q_2} \leq \frac{A_{sq,1}}{A_{sq,2}} \cdot \frac{L_{psv,1}/R_{a_1}}{L_{psv,2}/R_{a_2}} \tag{4}$$

We additionally note the width of the vapor channels has no impact on performance in our model. In loop heat pipe performance reporting, heat flow is generally reported as either a thermal conductance, in W/K, or its inverse, thermal resistance. This value directly describes the number of Watts transported by the device per Kelvin increase from the evaporator to the condenser. A larger value corresponds to more efficient heat transfer. This quantity is linearly proportional to q derived above from models of surface evaporation, and thus we expect $C_1/C_2 = q_1/q_2$.

3.3. An Interface-Focused Design Methodology

To maximize the efficiency of an LHP we focus on the interfacial design of the porous/solid region. For low powers, an optimally designed LHP should maximize the linear triple point contact between porous, solid, and vapor channels and aim to minimize the surface roughness of the solid wall to improve wetting.

Additionally, in medium-to-high power operating regimes, an optimally designed LHP should maximize the total solid/porous contact area, and minimize the capillary number for pores at these contact points. We demonstrate this approach by adding dispersed solid structures within the porous wick, aiming to maximize the contact regions across all domains, and, where possible, minimize surface roughness. While these interface optimizations have been noted as possible in prior literature [45], and improved wick wettability using adaptive particle morphology has provided notable improvements in traditionally manufactured LHPs[31, 50], the multiscale device-level optimizations identified in this work provide a pathway for substantial improvements in LHP performance independently from, and in addition to, other advances in wick properties.

4. Experimental Design

To test our design methodology, we manufacture and test two wick geometries. The first geometry consists of a standard LHP design, containing equally spaced porous pillars for evaporation. Our secondary design incorporates additional geometric features aiming to maximize the area for surface interactions, increasing the rate of evaporation for a given thermal load. These designs focus on maximizing evaporator heat transfer performance in a gravitational field, and do not incorporate a secondary wick, a required component for sustained microgravity operation. The lack of a secondary wick is not expected to have any effect on the heat transfer performance of the primary evaporator wick.

4.1. Manufacturing

NASA's Jet Propulsion Laboratory has developed porous manufacturing parameters of several alloys through laser powder bed fusion (LPBF)[26–28]. Using "Lack of Fusion" printing parameters and varying laser power, scan strategies, and layer thickness, additive manufacturing can achieve a similar microstructure to traditionally manufactured sintered wicks. Available materials include Nylon 11 (PA11), Al6061-RAM2, $AlSi_{10}Mg$, Ti-6Al-4V, SS316L, and Inconel 625. Of these materials, Ti-6Al-4V, SS316, and Inconel 625 are commonly used for LHP wicks. Ti-6Al-4V was selected for having the lowest thermal conductivity of available materials, minimizing undesirable heat leak across the wick into the compensation chamber as well as broad chemical compatibility. Evaporators are printed on an EOS M290. The outer housing uses standard printing settings for a fully dense part, while the porous wicks are engineered to have a permeability of 1.03×10^{-13}, a bubble point pore radius of $12.6\mu m$, and a porosity of 24.1%. We use a standard procedure for postprocessing additively manufactured titanium, including depowdering, heat treating, and removal from the build plate via wire EDM. A test manufacturing run is shown in Figure 6. This wick manufacturing

Figure 6: An in-process additive manufacturing run, showing 2 evaporator samples, as well as test coupons to verify print porosity and permeability (short rectangles), pore size (long rectangles), and electrical and thermal conductivity (small circles)

process was previously demonstrated for two-phase mechanically pumped loops[51, 52]. Mating surfaces, where the evaporators are connected to a system containing the vapor line, condenser, liquid return line, and compensation chamber are machined to meet specifications for two-ferrule compression tube fittings. Two of our test units are shown, post machining, in Figure 7. For research scale evaporator manufacturing, the total timeline from design to production is under 2 weeks, and the final evaporator cost, including depowdering and post-machining operations, is under $\$5000$.

Figure 7: Two Manufactured Evaporators

4.2. Evaporator Testing

A testing setup is constructed with 1000 mm of 3.18 mm OD/1.75 mm ID stainless steel tubing, connecting the vapor line of the evaporator to the condenser, 200 mm of 3.18 mm OD/1.75 mm ID serpentine stainless steel tubing as the condenser, an additional 1000 mm of 6.35mm OD/4.6mm ID stainless steel tubing connecting the condenser outlet to 50 mm length by 10mm ID stainless steel tubing compensation chamber, which flows back into the evaporator. The compensation chamber is fitted with a T junction, to allow for filling the device. Thermocouples are mounted at several points on the evaporator, the vapor line, the condenser, and the liquid return line. The bottom of the compensation chamber is connected to the center of evaporator, and the vapor line is connected to side outlet from the evaporator. Additional components, such as pressure gauges or pressure relief valves may be connected to the opposite side outlet from the evaporator. A schematic of the test setup with thermocouple locations is given in Figure 8, and a version of this test setup using clear liquid and vapor lines to visualize fluid flow is shown in Figure 9. Charging is performed by initially vacuuming the internal system pressure to 10^{-4}MPa to eliminate non-condensible gas contamination. Forty percent of the system's volume is then filled with acetone. Although it is not the optimal working fluid for heat transfer, acetone was selected due to its operating range between $50°C - 150°C$, matching the cooling needs of common electronic systems. Acetone further provides additional safety for new device testing, with low toxicity and a low pressure critical point.

5. Results

To enable equitable comparison between our optimized and traditional designs, evaporators are evaluated across the performance range of 20-70W power input. Both evaporators have a total cross sectional area of $3.96cm \times 3.96cm$, and heat is applied using a heater with a cross sectional area of $1.266cm^2$. This

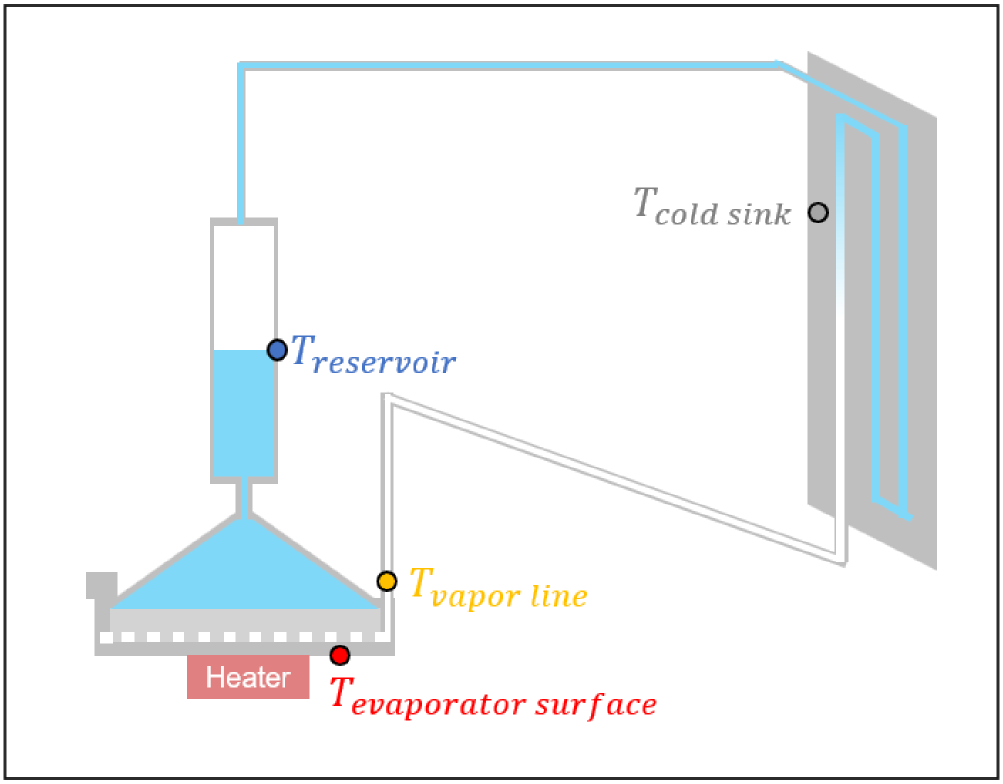

Figure 8: A schematic of our test setup and thermocouple locations

corresponds to a local heat flux from 15.8-55.3W/cm^2, and an average heat flux, accounting for the total wick surface area, from 1.3-4.5W/cm^2.

5.1. Evaporator Designs

Our traditional design contains no surface optimization or design geometry optimization. The wick interfaces with the solid housing using porous pillars in a hexagonally packed circle arrangement. The surface roughness of the porous/solid interface is $R_a = 15.46\mu m$ with a standard deviation of $3.77\mu m$. In our optimized design, we heuristically apply our numerical lessons from Section 3.3 to improve contact area within the evaporator. We develop a 3-dimensional wick structure to maximize both the total available solid/porous interface for menisci to form, and which contains areas with improved thin-film wetting properties. The optimized wick contains 74cm of linear contact area with an average surface roughness $R_a = 15.46\mu m$ with a standard deviation of $3.77\mu m$, and additionally contains 52.6cm of linear contact area with an average surface roughness of $R_a = 9.85\mu m$ and a standard deviation of $1.15\mu m$. These geometric wick optimizations are done without any modifications to the geometry of the housing, the thickness of the wick, or the porosity/permeability of the wick. The full area and surface roughness measurements of both

Table 1: Wick geometry and roughness parameters

Design	Surface	A_{sq} [cm^2]	L_{psv} [cm]	R_a [µm]	L_{psv}/R_a
Traditional	Upskin	6.2	133.0	15.46	8.60
Optimized	Upskin	3.8	74.0	15.46	4.79
	Vertical z	4.2	52.6	9.85	5.34

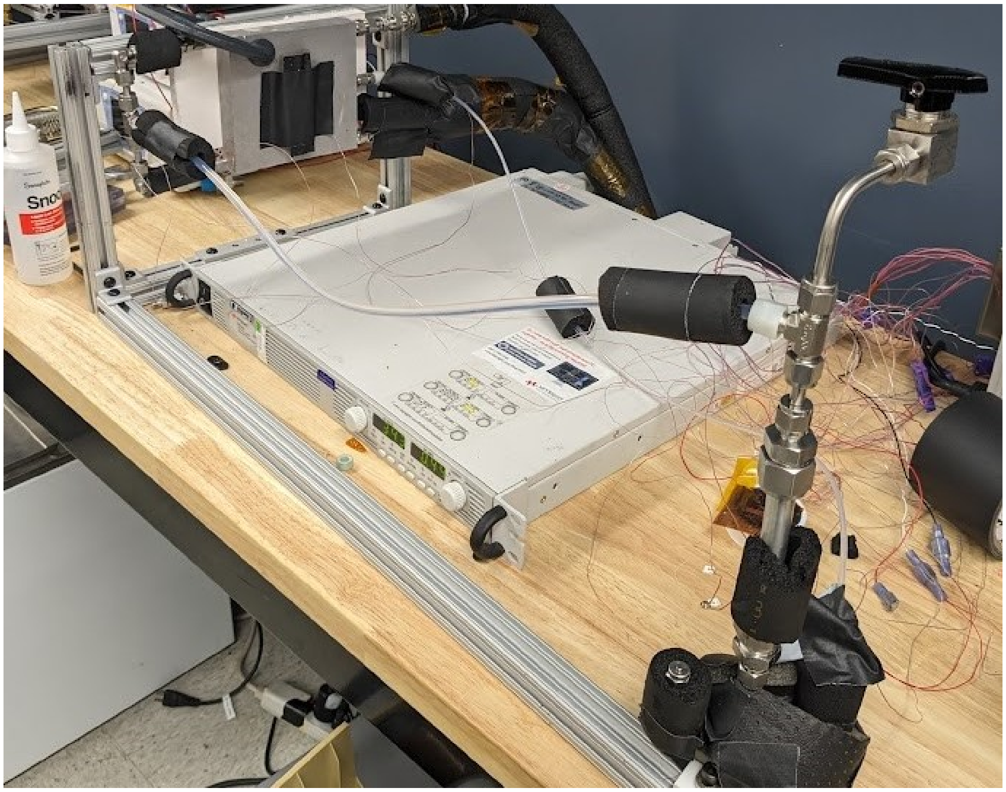

Figure 9: Tabletop LHP testing setup with clear adiabatic lines to visualize flow.

the traditional and optimized designs is given in Table 1, and a cross section of both evaporators is shown in Figure 10. Putting these parameters into Equation 4 provides a predicted performance improvement for the optimized device with a lower bound of 17.7% and an upper bound of 51.9%.

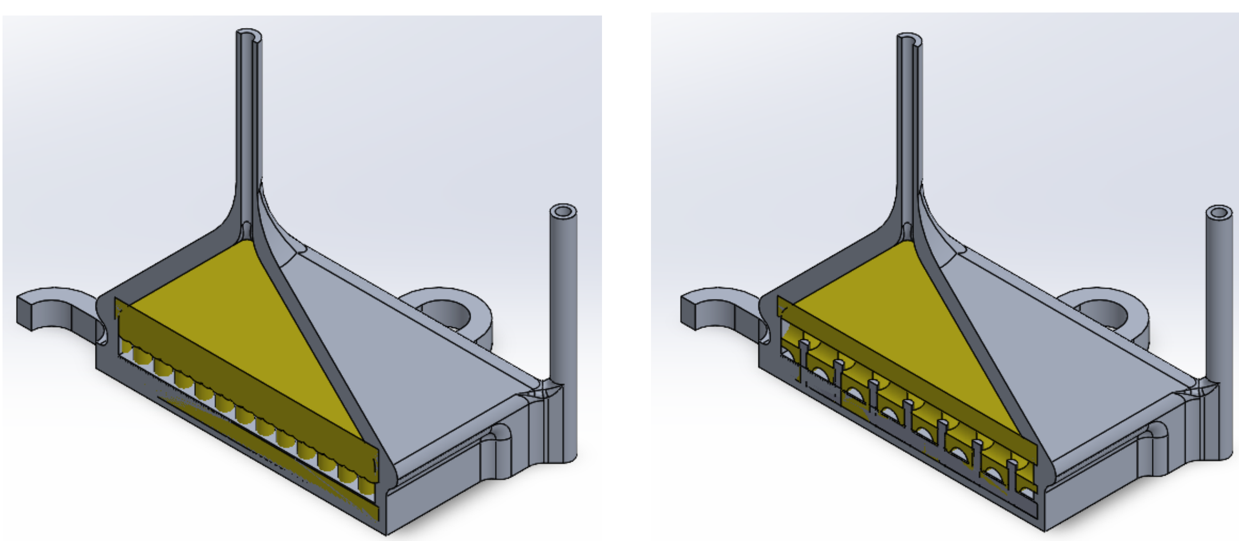

(a) Our Hexagonal Circle Packed Wick

(b) Our 3D architected wick

Figure 10: Section views of our wick architectures.

We conduct characterization testing over the standardized range of 20-$70W$, with a cold sink regulated to $25°C$. For the unoptimized design, we find a maximum evaporator temperature of $198°C$ at $70W$ power input, while the optimized evaporator reaches a maximum temperature of $150°C$ at the same power. The full preliminary characterization testing for both devices is shown in Figure 11. Further characterization tests of

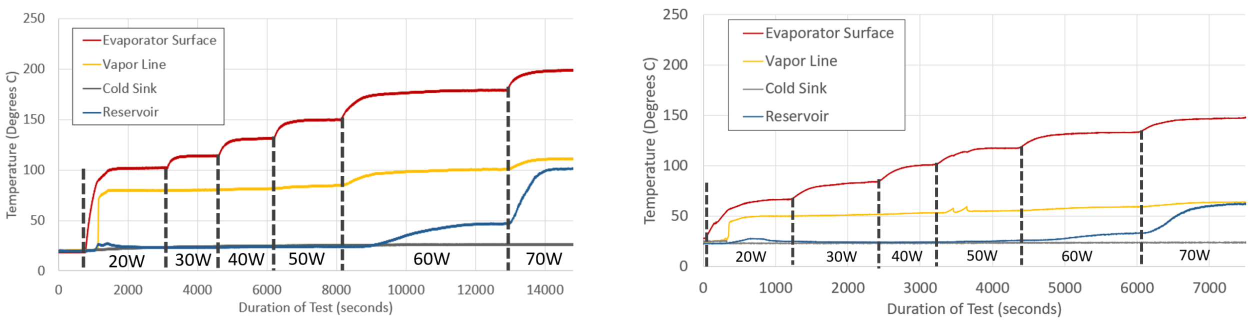

(a) Standard Geometry LHP

(b) Optimized Geometry LHP

Figure 11: Preliminary Characterization Tests for LHP evaporators

the optimized design, including analysis of low power startup and hysteresis characterization are provided in Appendix A.

5.2. Discussion

We begin by noting the similarities in performance characteristics between the two evaporators. Both tests begin with the evaporator surface heating up, as power is applied to the wick. "Startup", the point where vapor first starts evaporating from the wick surface, is marked by the sharp increase in the vapor line temperature, where hot vapor begins traveling to the condenser. For both versions of the evaporator, we see a slight increase in reservoir temperature during startup, which returns to equilibrium after startup is reached. We begin the test at 20W, and hold power constant until the LHP reaches an equilibrium state. For both trials, upon reaching 60W, we see a slight increase compensation chamber temperature, as well as a slight increase in vapor temperature, both corresponding to heat leak through the wick, a common problem in additively manufactured LHPs. This increase in temperature occurs again at 70W, where the temperature of the compensation chamber nearly reaches the vapor temperature, as heat leak continues. However, even at these elevated temperatures, both devices reach equilibrium at 70W. We note a persistently slightly longer time to reach equilibrium at new power levels for the standard geometry LHP. We expect this is due to a larger change in temperature between each equilibrium states. Additionally, for this trial of the optimized design, we observe a slight instability in vapor temperature occurs at 50W, however this instability disappears before reaching equilibrium.

The primary difference between these LHP designs is the temperature of the evaporator surface as power increases. To compare these temperatures, we compute the conductance of each LHP, given in W/K by $Q_{input}/(T_{evaporator} - T_{condenser})$. Using the values listed in section 5.1, we find an upper bound expected performance differential of 51.9%, and a lower bound of 17.7%. Across the tested range from 20 to $70W$, the conductance of the standard geometry ranges from $0.25W/K$ to $0.40W/K$, while the optimized design geometry conductance ranges from $0.41W/K$ to $0.60W/K$. These values correspond to a 42% average performance improvement, with a range from 33% to 53%, for the optimized design. The full range of conductance for our tests is shown in Figure 12. This observed performance improvement is at the upper end of our predicted performance improvement, from 17.7% to 51.9%. While the true performance improvement slightly exceeds the upper bound from our simple predictive model, the general agreement indicates our model and design methodology captures the dominant variables for additively manufactured LHP optimization. Our data further suggests that both predicted effects are simultaneously active for the majority of the operating

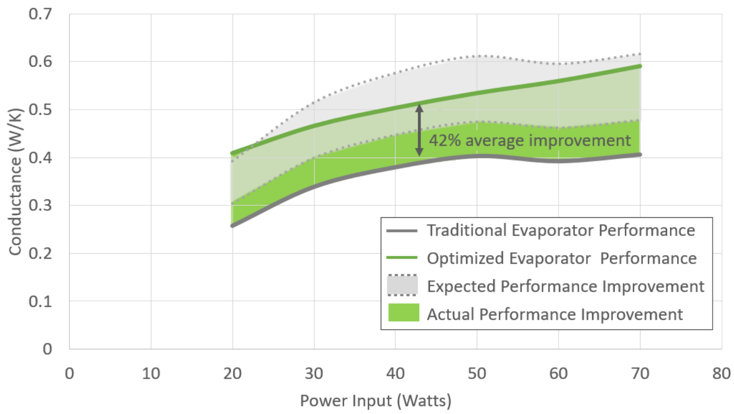

Figure 12: Raw conductance for Optimized Designs vs Unoptimized Designs across a test range of input powers

regime. Additional variables not considered in our initial modeling of the system include the quantity of dissolved gasses in the working fluid, dynamic effects of vapor pocket formation on rough surfaces, and other nonlinear and second-order effects on evaporation rate and heat pipe performance. The importance of low-roughness surfaces is expected to be amplified in LHPs operating with working fluids of high surface tension, such as water, where hydrogen bonding reduces wetting potential relative to refrigerants. Additionally, these effects of wetting behavior and surface roughness are likely applicable to to other wick-type evaporators, including in refrigeration cycles, traditional heat pipes, and two-phase mechanically pumped loops.

5.3. Loop Conductance

The additively manufactured evaporators were designed to meet safety specifications for new untested pressure vessels. To meet these standards, the exterior wall thickness was selected to withhold $9.38MPa$, double the critical pressure of our chosen working fluid, acetone. Due to these safety considerations, a significant portion of the measured thermal gradient (up to $80°C$ at higher powers) is across the 6.35mm thick evaporator wall. To directly compare wick performance, we additionally compute the conductance using the interior wall temperature. We predict this interior wall temperature using a constant conductance plate, which is a sufficient approximation for a flat plate LHP, and verify its accuracy using thermocouple measurements from the beginning of the vapor line. We find agreement between these approaches within 10%. For our tested range, we find an average loop conductance of $0.81W/K$ for the unoptimized design and $1.26W/K$ for the optimized design. This loop conductance can be viewed as an upper limit for the specific tested evaporator design, which can be approached at a system conductance level through dedicated efforts to minimize the outside wall thickness.

5.4. Sample Variation

Loop heat pipes traditionally have significant performance variations across manufactured devices. To demonstrate that the enhanced performance of the optimized device is repeatable, we manufacture two additional samples. These additional samples are manufactured in different builds, with different batches of titanium powder, on different locations in the build plate in the same EOS M290 machine. We find an average variation across these samples of just 7%. The loop conductance versus power input for three optimized devices is shown in Figure 13. While the additive manufacturing process for our evaporators is consistent, remaining potential sources of variance include position and orientation on the build plate, variance in the powder feedstock, and variations in charging and assembly, such as purity of the working fluid, variations within the vacuum quality, and quality of contact between the heater and evaporator housing. Of these potential sources of variance, we intentionally selected different powder feedstock sources and different

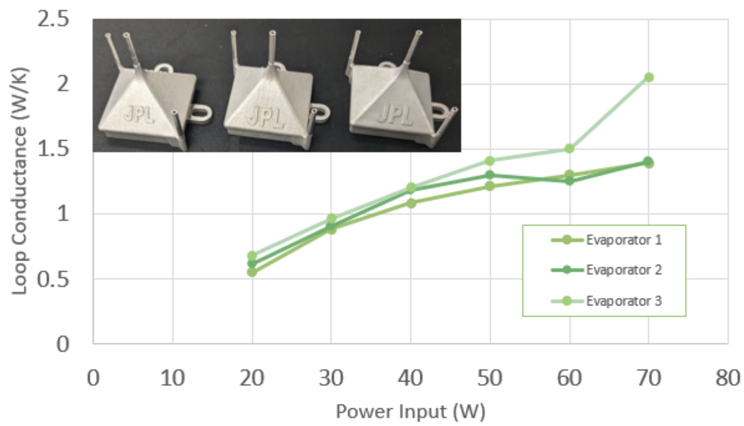

Figure 13: Loop Conductance versus input power for three evaporator samples

locations on the build plate, and tested the devices on different days, where local air pressure and humidity may have effected charging and fluid characteristics. Regardless, the observed variance is significantly below the variance of traditionally manufactured LHPs, where performance is often dependent on a diverse array of manufacturing challenges[36].

5.5. Literature Comparison

Testing of LHPs is not standardized across the literature. To provide a point of comparison, we refer to Wang (2019)[53]. This work tests an acetone LHP with $500mm$ long vapor and liquid lines, half of the heat transport distance demonstrated with our additively manufactured design. We provide a comparison to the results for a $2mm$ ID vapor line, chosen due to its proximity to our $1.75mm$ ID vapor line, in Table 2. While

Table 2: Performance Comparison to an Acetone LHP from literature

Design	Wick Porosity	Wick Pore Size	Avg. Conductance 30-60W
Traditional Design	24.1%	12.6μm	$0.43W/K$
Optimized Design	24.1%	12.6μm	$0.51W/K$
Wang (2019)[53]	55%	0.53μm	$0.50W/K$

differences in the exact testing setup make direct comparison between evaporators difficult, these results indicate that our optimized evaporator design provides effective long distance heat transfer, with comparable conductance to shorter-distance traditional designs from the literature, in spite of the lower porosity and larger pore size of our wick.

6. Conclusion

LHPs have long served as a gold standard for passive long-distance heat transfer. While low cost additively manufactured LHPs traditionally suffer a performance penalty which limiting their adoption in large-scale satellite swarms, disposable missions, and terrestrial industrial cooling, we have developed a design methodology to significantly improve the performance of these devices. With the advances presented in this paper, AM LHPs preserve the long-term space mission level reliability of traditional LHPs without the traditional performance sacrifice due to the established porosity/permeability tradeoff. This advancement immediately extends the viable range for LHPs from high-cost satellites to include fleet-level adoption in cubesats and internet satellites, while illustrating a clear path for LHP development as a drop-in replacement for existing datacenter and terrestrial computing applications, where LHPs have the potential to save as up to 30% of cooling power[9, 20]. Additionally, the lessons learned in optimizing surface interactions extend to other existing two-phase heat transfer devices, enabling high-efficiency heat transfer with large-pore wicks, including mechanically pumped two-phase loops and some refrigeration cycles, where architected wick designs may significantly improve energy efficiency and performance. Further work and future developments include computational optimization of the effects identified in this work using emerging ML methods, improved wick manufacturing processes and application-specific design considerations, such as working fluid, weight requirements, and optimization for specific heat loads.

Acknowledgments

This work was supported by the NASA Jet Propulsion Laboratory's Research and Technology Development Program. The research was carried out at the Jet Propulsion Laboratory, California Institute of Technology, under contract with the National Aeronautics and Space Administration (80NM0018D0004). The authors acknowledge the JPL Advanced Thermal Technology Lab for support in device testing, and the JPL Additive Manufacturing Center for support in manufacturing. The supplemental dataset included in Appendix A was curated by Takeshi Yokouchi from Tohoku University, Japan.

Author Contributions

KP: Investigation, Data curation, Methodology, Formal Analysis, Visualization, Writing – original draft. SR: Conceptualization, Funding acquisition, Formal Analysis, Visualization, Project administration, Writing - review & editing.

Declaration of Competing Interests

K. Piper and S.N. Roberts are named inventors on a provisional patent, assigned to the California Institute of Technology, which contains some design considerations described in this article. S.N. Roberts is a named inventor on U.S. Patent US10746475B2, assigned to the California Institute of Technology, which relates to the manufacturing methods from this article.

References

[1] G. Sachs, "Ai poised to drive 160% increase in power demand," *Goldman Sachs*, 2023.

[2] L. Riahi, O. Abdelaziz, R. Gluckman, I. Hamilton, and W. T. L. Chow, "Global cooling watch 2025," *United Nations Environment Programme*, 2025.

[3] J. Liu, N. qiang Pei, K. hua Guo, Z. hui He, T. xuen Li, and M. Lv, "Experimental investigation on mechanical pumped cooling loop for application in future space missions," *Energy Conversion and Management*, vol. 49, no. 10, pp. 2704–2710, 2008.

[4] A. Heydari, O. Al-Zu'bi, Y. Manaserh, A. R. Gharaibeh, R. Tipton, M. Mehrabikermani, J. Rodriguez, and B. Sammakia, "Advancing in data centers thermal management: Experimental assessment of two-phase liquid cooling technology," *Journal of Electronic Packaging*, vol. 147, no. 4, p. 041108, 2025.

[5] E. D. Cartwright, "The environmental justice and community impacts of data centers," 2026.

[6] T. Feng, Y. Pei, H. Zhang, B. Asai, G. Dong, A. Joshi, A. Saha, S. Cai, and R. Chen, "High-flux and stable thin-film evaporation from fiber membranes with interconnected pores," *Joule*, vol. 9, no. 7, 2025.

[7] H. Yin, G. Gao, K. Liu, Y. Yang, G. Wu, and J. Ren, "Decomposition properties of two phase immersion cooling medium c6f12o: A computational study," *Chemical Physics Letters*, vol. 794, p. 139505, 2022.

[8] C. Zhang, H. Wang, Y. Huang, L. Zhang, and Y. Chen, "Immersion liquid cooling for electronics: Materials, systems, applications and prospects," *Renewable and Sustainable Energy Reviews*, vol. 208, p. 114989, 2025.

[9] T. Ding, X. Chen, H. Cao, Z. He, J. Wang, and Z. Li, "Principles of loop thermosyphon and its application in data center cooling systems: A review," *Renewable and Sustainable Energy Reviews*, vol. 150, p. 111389, 2021.

[10] G. Y. Eastman, "The heat pipe," *Scientific American*, p. All, 1968.

[11] P. D. Dunn and D. A. Reay, "The heat pipe," *Physics in Technology*, p. All, 1973.

[12] S. A. Said and B. A. Akash, "Experimental performance of a heat pipe," *Elsevier International Communications in Heat and Mass Transfer*, vol. 26, p. All, 1999.

[13] M. G. Mwaba, X. Huang, and J. Gu, "Influence of wick characteristics on heat pipe performance," *International Journal of Energy Research*, p. All, 2006.

[14] W. Anderson, P. Dussinger, S. Garner, J. Hartenstine, and D. Saraff, "Loop heat pipe design, manufacturing, and testing: an industrial perspective," in *Heat Transfer Summer Conference*, vol. 43581, pp. 497–503, 2009.

[15] B.-J. Huang, Y.-H. Chuang, and P.-E. Yang, "Low-cost manufacturing of loop heat pipe for commercial applications," *Applied Thermal Engineering*, vol. 126, pp. 1091–1097, 2017.

[16] L. Bai, J. Fu, G. Lin, C. Zhou, and D. Wen, "Quiet power-free cooling system enabled by loop heat pipe," *Applied Thermal Engineering*, vol. 155, pp. 14–23, 2019.

[17] Y. Guo, G. Lin, J. He, L. Bai, Y. Sun, H. Zhang, and J. Miao, "Experimental analysis of operation failure for a neon cryogenic loop heat pipe," *International Journal of Heat and Mass Transfer*, vol. 138, pp. 96–108, 2019.

[18] L. Bai, L. Zhang, G. Lin, J. He, and D. Wen, "Development of cryogenic loop heat pipes: A review and comparative analysis," *Applied Thermal Engineering*, vol. 89, pp. 180–191, 2015.

[19] H. Zhang, Y. Tian, C. Tian, and Z. Zhai, "Effect of key structure and working condition parameters on a compact flat-evaporator loop heat pipe for chip cooling of data centers," *Energy*, vol. 284, p. 128658, 2023.

[20] F. Zhou, C. Li, W. Zhu, J. Zhou, G. Ma, and Z. Liu, "Energy-saving analysis of a case data center with a pump-driven loop heat pipe system in different climate regions in china," *Energy and Buildings*, vol. 169, pp. 295–304, 2018.

[21] L. Franceschetti, Y. Kameya, and M. Kaviany, "3d-printed, ceramic porous metasurface wick: Hexagonal-prism unit-cell capillary evaporator," *International Journal of Heat and Mass Transfer*, vol. 246, p. 127041, 2025.

[22] Y. Kameya, Y. Takahashi, and M. Kaviany, “Surface evaporation enhancement using porous metasurfaces: 3-d multiscale, open-system wick evaporators,” *International Journal of Heat and Mass Transfer*, vol. 216, p. 124605, 2023.

[23] S. Morris, “The evaporating meniscus in a channel,” *Journal of Fluid Mechanics*, vol. 494, pp. 297–317, 2003.

[24] L. Swanson and G. Herdt, “Model of the evaporating meniscus in a capillary tube,” 1992.

[25] R. Rand, “The dynamics of an evaporating meniseus,” *Acta Mechanica*, vol. 29, no. 1, pp. 135–146, 1978.

[26] R. Gotoh *et al.*, “Experimental and analytical investigations of alsi10mg, stainless steel, inconel 625 and ti-6al-4v porous materials printed via powder bed fusion, prog. addit. manuf.(progress in additive manufacturing) 7 (5)(2022) 943–955.”

[27] D. Oropeza, T. Seager, S. Firdosy, H. Tran, T. Schrand, and N. Sridharan, “Porosity control of copper-based alloys via powder bed fusion additive manufacturing for spacecraft applications,” *Journal of Porous Materials*, vol. 31, pp. 779–791, 2024.

[28] L. Valdarno, V. K. Dhir, B. Furst, and E. Sunada, “Numerical and experimental investigation of heat transfer in the porous media of an additively manufactured evaporator of a two-phase mechanically pumped loop for space applications,” *Microgravity Science and Technology*, vol. 36, 2024.

[29] R. Singh, A. Akbarzadeh, and M. Mochizuki, “Effect of wick characteristics on the thermal performance of the miniature loop heat pipe,” 2009.

[30] Y. Qu, S. Wang, and Y. Tian, “A review of thermal performance in multiple evaporators loop heat pipe,” *Applied Thermal Engineering*, vol. 143, pp. 209–224, 2018.

[31] H. Guo, X. Ji, Y. Gan, and J. Xu, “Experimental study on the heat transfer performance of loop heat pipe with different particle morphology and wettability of porous wick,” *International Journal of Thermal Sciences*, vol. 186, p. 108134, 2023.

[32] R. Singh, A. Akbarzadeh, C. Dixon, M. Mochizuki, and R. R. Riehl, “Miniature loop heat pipe with flat evaporator for cooling computer cpu,” *IEEE Transactions on Components and Packaging Technologies*, vol. 30, no. 1, pp. 42–49, 2007.

[33] P. Szymanski, D. Mikielewicz, and S. Fooladpanjeh, “Current trends in wick structure construction in loop heat pipes applications: a review,” *Materials*, vol. 15, no. 16, p. 5765, 2022.

[34] S. Launay, V. Sartre, and J. Bonjour, “Parametric analysis of loop heat pipe operation: a literature review,” *International Journal of Thermal Sciences*, vol. 46, no. 7, pp. 621–636, 2007.

[35] B. Richard, W. G. Anderson, and J. Crawmer, “Development of a 3d printed loop heat pipe,” in *2019 35th Semiconductor Thermal Measurement, Modeling and Management Symposium (SEMI-THERM)*, pp. 58–60, IEEE, 2019.

[36] A. Ambirajan, A. A. Adoni, J. S. Vaidya, A. A. Rajendran, D. Kumar, and P. Dutta, “Loop heat pipes: a review of fundamentals, operation, and design,” *Heat Transfer Engineering*, vol. 33, no. 4-5, pp. 387–405, 2012.

[37] L. Vasiliev, D. Lossouarn, C. Romestant, A. Alexandre, Y. Bertin, Y. Piatsiushyk, and V. Romanenkov, "Loop heat pipe for cooling of high-power electronic components," *International Journal of Heat and Mass Transfer*, vol. 52, no. 1-2, pp. 301–308, 2009.

[38] D. Jafari, W. W. Wits, and B. J. Geurts, "Phase change heat transfer characteristics of an additively manufactured wick for heat pipe applications," *Applied thermal engineering*, vol. 168, p. 114890, 2020.

[39] J. Ferreira, M. Kaviany, V. Dupont, O. de Laet, T. Nicolle, and E. Yen, "A loop heat pipe for vehicle cpu cooling: Peak performance and partial flooding and dryout regimes," in *Heat Transfer Summer Conference*, vol. 85796, p. V001T16A001, American Society of Mechanical Engineers, 2022.

[40] K. Odagiri and H. Nagano, "Heat transfer characteristics of flat evaporator loop heat pipe under high heat flux condition with different orientations," *Applied Thermal Engineering*, vol. 153, pp. 828–836, 2019.

[41] J. Esarte, J. Blanco, A. Bernardini, and J. San-José, "Optimizing the design of a two-phase cooling system loop heat pipe: Wick manufacturing with the 3d selective laser melting printing technique and prototype testing," *Applied Thermal Engineering*, vol. 111, pp. 407–419, 2017.

[42] P. Szymanski and D. Mikielewicz, "Additive manufacturing as a solution to challenges associated with heat pipe production," *Materials*, vol. 15, no. 4, p. 1609, 2022.

[43] J. Schonberg, S. DasGupta, and P. Wayner Jr, "An augmented young-laplace model of an evaporating meniscus in a microchannel with high heat flux," *Experimental thermal and fluid science*, vol. 10, no. 2, pp. 163–170, 1995.

[44] M. Hamdan and E. Elnajjar, "Thermodynamic analytical model of a loop heat pipe," *Heat and mass transfer*, vol. 46, no. 2, pp. 167–173, 2009.

[45] S. Launay and M. Vallée, "State-of-the-art experimental studies on loop heat pipes," *Frontiers in Heat Pipes (FHP)*, vol. 2, no. 1, 2011.

[46] Y. Akizuki, K. Odagiri, K. Sawada, H. Yoshizaki, M. Sairaiji, and H. Ogawa, "Heat transport characterization on different orientations of a loop heat pipe with an additive manufactured evaporator," *Applied Thermal Engineering*, vol. 264, p. 125455, 2025.

[47] X. Xie, Q. Weng, Z. Luo, J. Long, and X. Wei, "Thermal performance of the flat micro-heat pipe with the wettability gradient surface by laser fabrication," *International Journal of Heat and Mass Transfer*, vol. 125, pp. 658–669, 2018.

[48] R. N. Wenzel, "Resistance of solid surfaces to wetting by water," *Industrial & engineering chemistry*, vol. 28, no. 8, pp. 988–994, 1936.

[49] Y. Deng, C. Peng, M. Dai, D. Lin, I. Ali, S. S. Alhewairini, X. Zheng, G. Chen, J. Li, and I. Naz, "Recent development of super-wettable materials and their applications in oil-water separation," *Journal of Cleaner Production*, vol. 266, p. 121624, 2020.

[50] Y. Zhang, J. Liu, J. Wang, T. Luan, H. Chen, and H. Xue, "Experimental study on the characteristics of loop heat pipe with modified carbon fiber felt wick," *Applied Thermal Engineering*, vol. 234, p. 121239, 2023.

[51] B. Furst, S. Cappucci, T. Daimaru, E. Sunada, S. Roberts, and T. O'Donnell, "An additively manufactured evaporator with integrated porous structures for two-phase thermal control," 48th International Conference on Environmental Systems, 2018.

[52] J. Ferreira, B. Furst, T. Daimaru, E. Sunada, and M. Kaviany, "Analytic characterization and operational limits of a hybrid two-phase mechanically pumped fluid loop based on the capillary pumped loop," *International Journal of Heat and Mass Transfer*, vol. 183, p. 122019, 2022.

[53] H. Wang, G. Lin, L. Bai, J. Fu, and D. Wen, "Experimental study on an acetone-charged loop heat pipe with a nickel wick," *International Journal of Thermal Sciences*, vol. 146, p. 106104, 2019.

Appendix A. Additional Characterization Testing of Optimized Evaporator

Appendix A.1. Thermocouple Layout 1

The tests in this section (Figures A.14 - A.19) are performed with a vapor and liquid line of 600mm length, and a condenser length of 550mm. The liquid, vapor, and condenser lines all have an ID of 1.75mm. The thermocouple layout for all tests in this section is shown in Figure A.14.

Appendix A.2. Thermocouple Layout 2

Tests in this section (Figures A.20 onwards) use a new measurement location for the evaporator housing thermocouple, shown in Figure A.20. Otherwise, the test setup remains unchanged from the previous section, maintaining a vapor and liquid line of 600mm length, and a condenser length of 550mm.

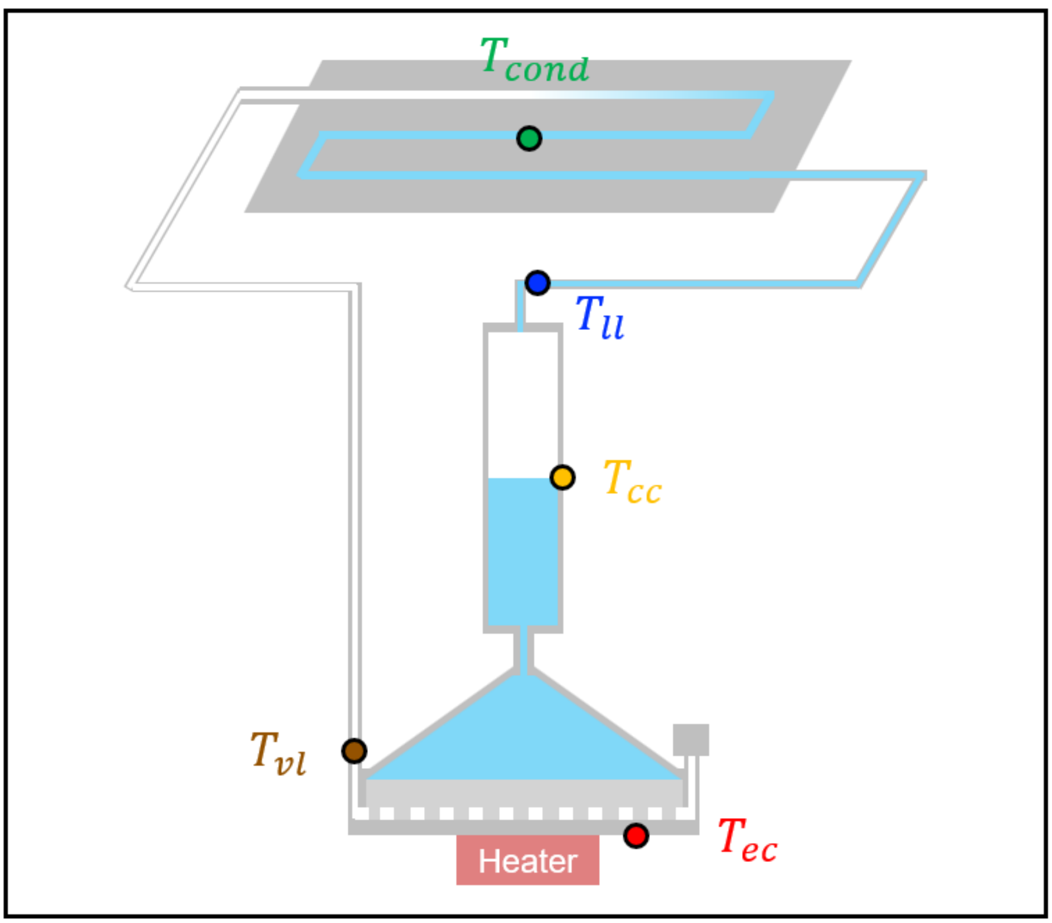

Figure A.14: Locations for Thermocouples

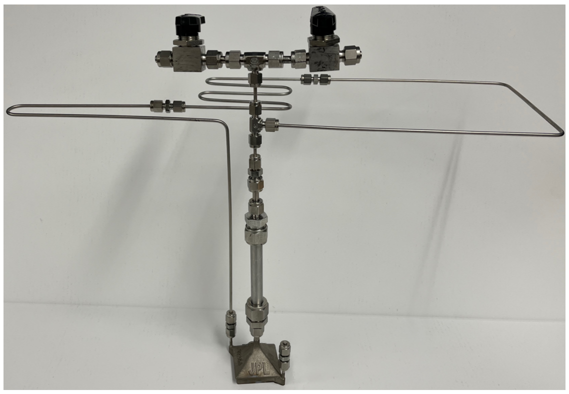

(a) The uninsulated test setup

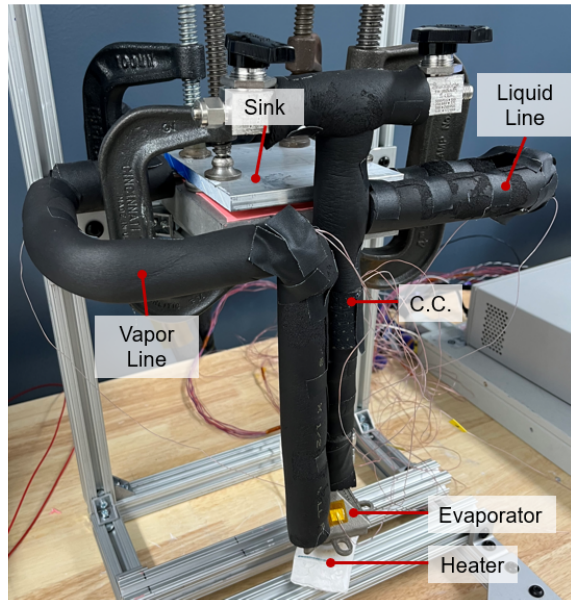

(b) The insulated test setup

Figure A.15: Testing Setup for Appendix A Data

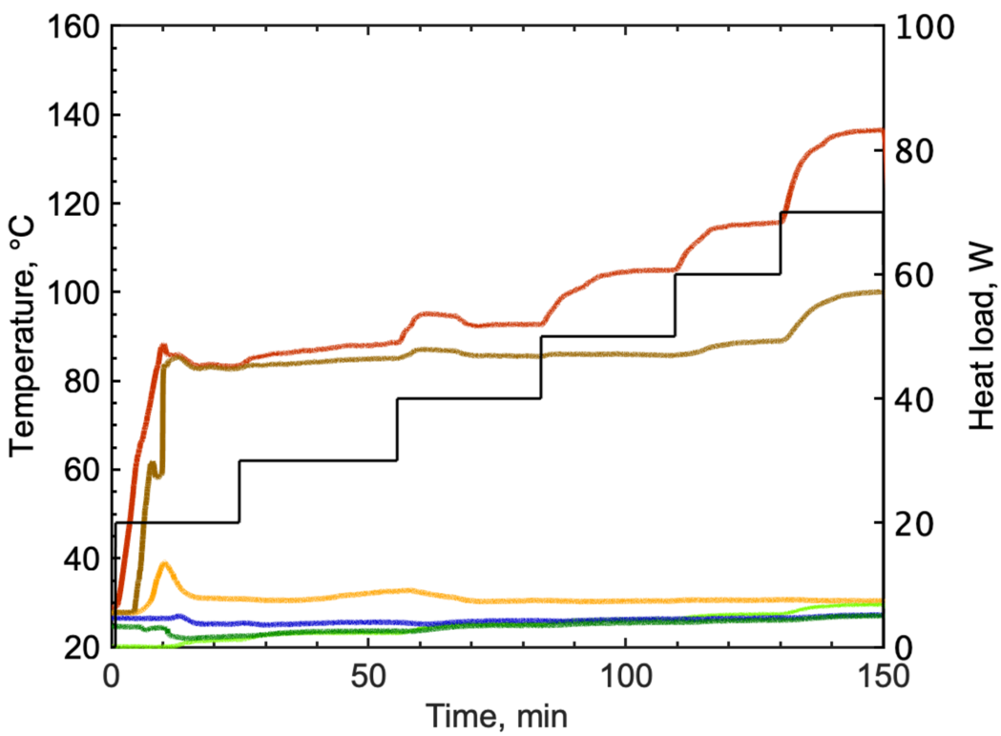

Figure A.16: Characterization Test Up to 70W

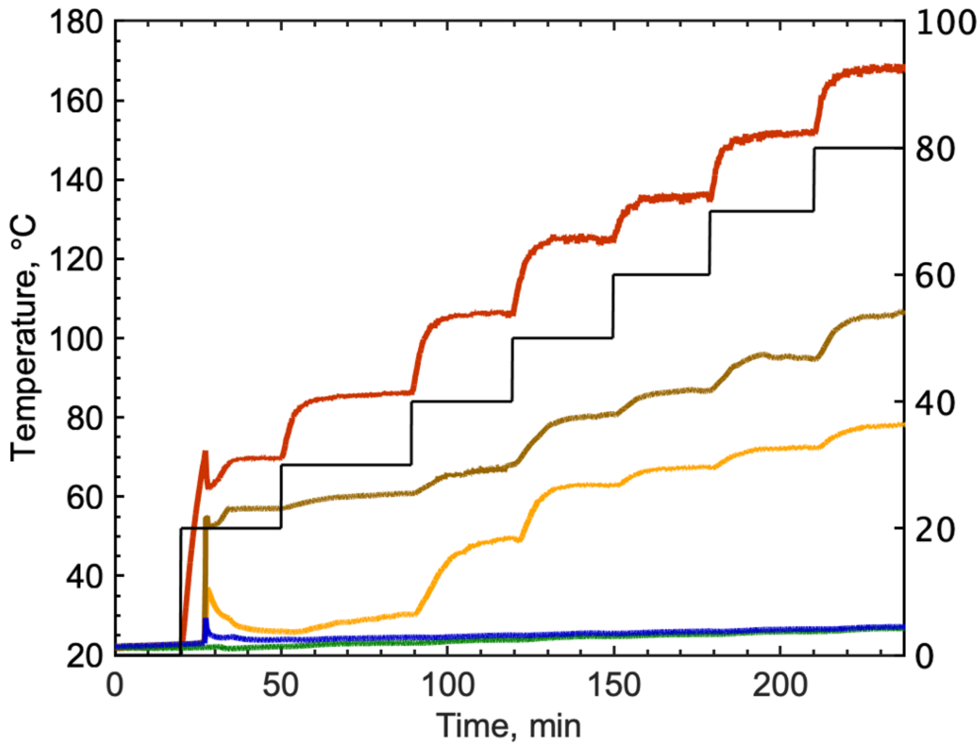

Figure A.17: Characterization Test Up to 80W

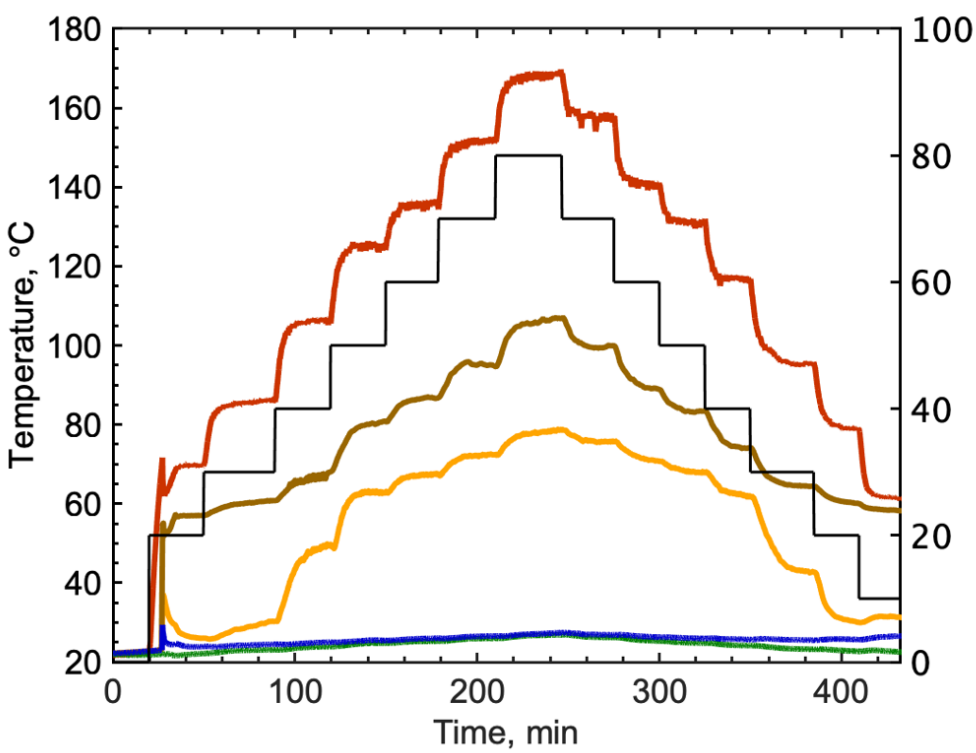

Figure A.18: Hysteresis Characterization Test

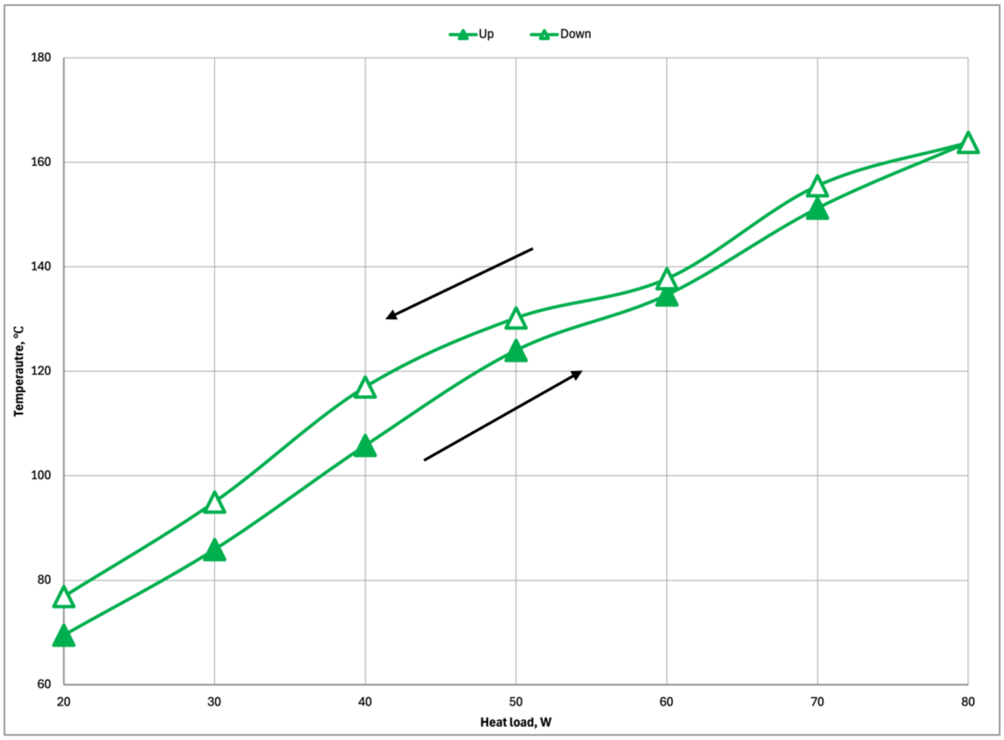

Figure A.19: Hysteresis Characterization Test

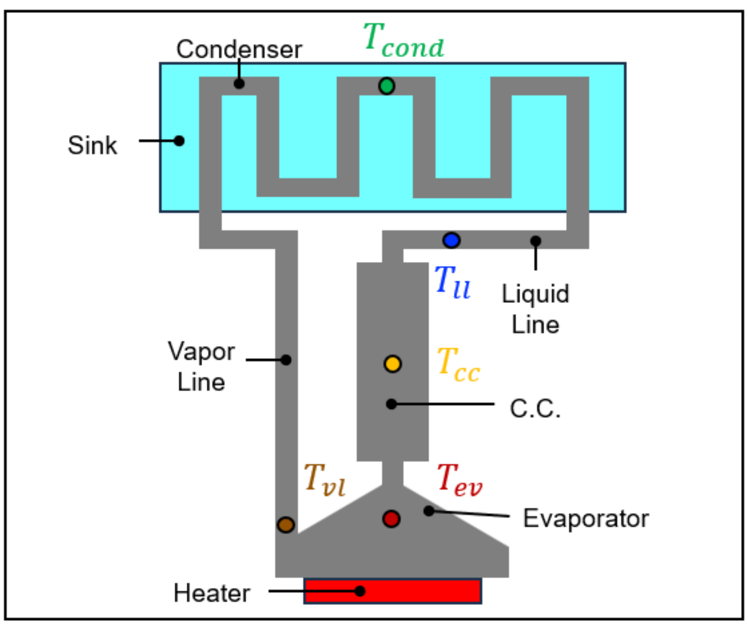

Figure A.20: Locations for Thermocouples

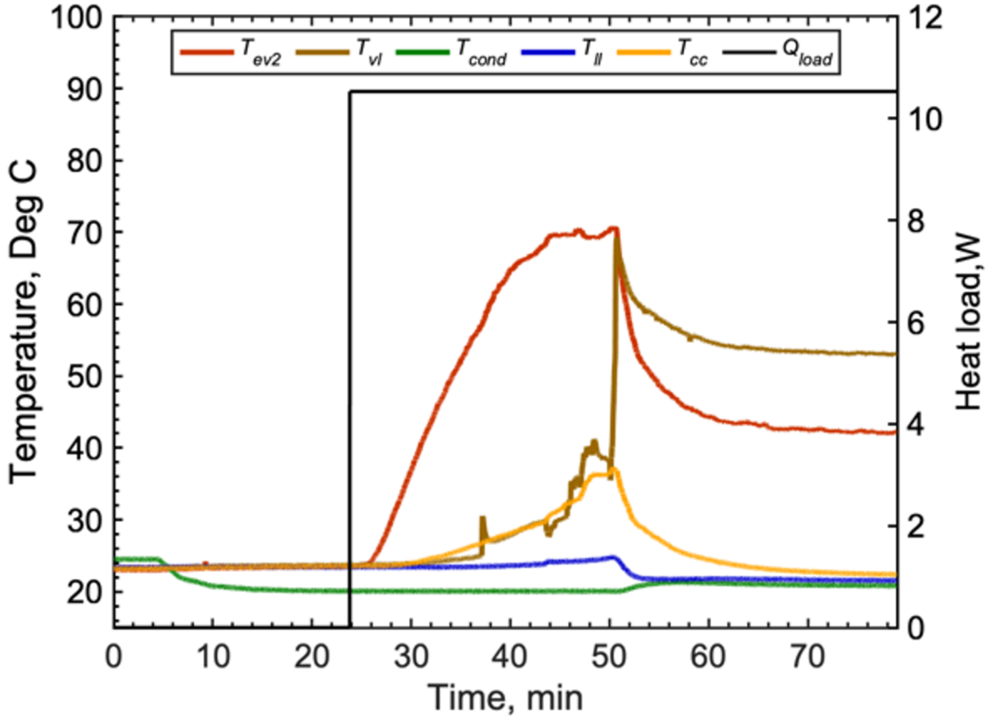

Figure A.21: Start Up Characterization at 10W

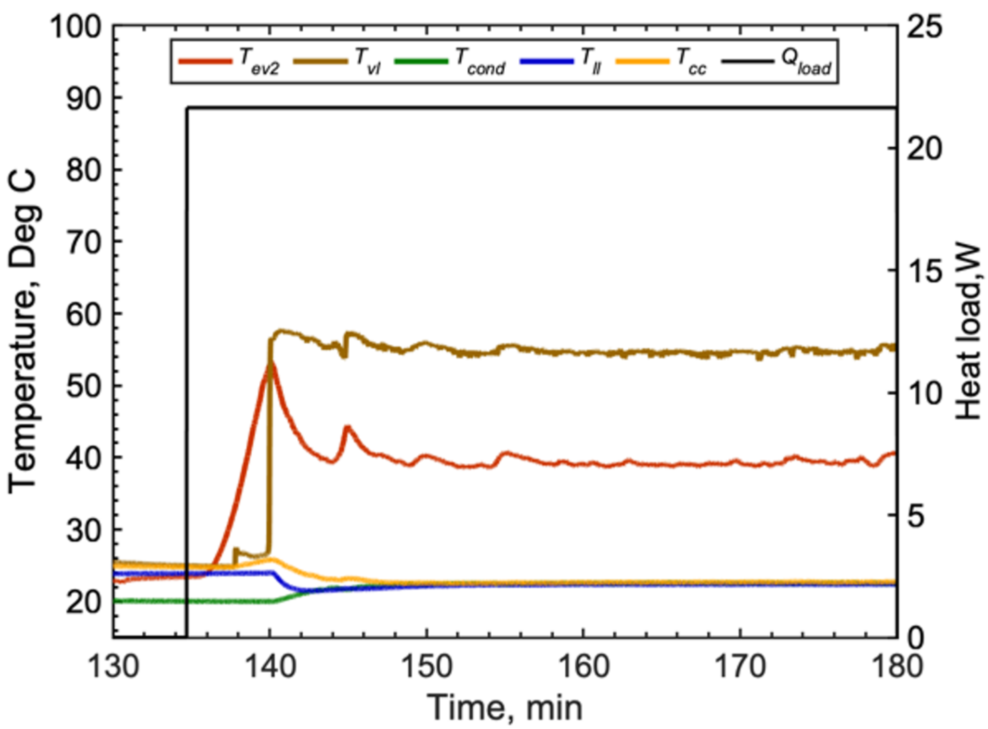

Figure A.22: Start Up Characterization at 20W

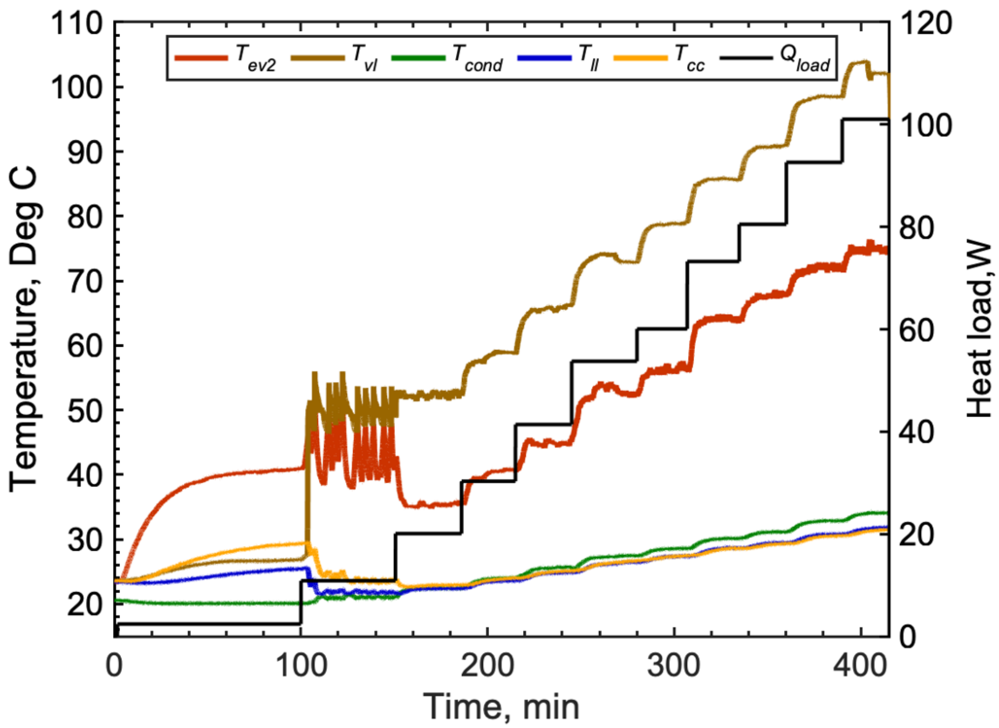

Figure A.23: Characterization Testing up to 100W